

## Chapter 3

# Quasiparticle Interference

This chapter details the use of Fourier-transform scanning tunneling spectroscopy (FT-STTS) to yield simultaneous real space and momentum space information in the high temperature superconductor  $\text{Bi}_2\text{Sr}_2\text{CaCu}_2\text{O}_{8+\delta}$  (BSCCO). Because quasiparticles in BSCCO are both inhomogeneous and highly correlated, a full understanding of their properties will require knowledge of both their  $\vec{R}$ -space and  $\vec{k}$ -space behavior. This work represents the first application of FT-STTS to a cuprate superconductor. The trick of this analysis technique is to take advantage of scattering, which leads to interference patterns in the quasiparticle density of states that can be imaged with scanning tunneling microscopy and spectroscopy. By Fourier-transforming then inverting the real-space interference patterns, we can access the  $\vec{k}$ -space information in the sample.

In this work, FT-STTS is applied to optimally doped BSCCO samples at  $T = 4.2$  K, with  $B = 0$  Tesla. The BSCCO phase space explored in this chapter is shown in figure 3.1.

### 3.1 Basic Scattering Explanation

In an ideal metal, the Landau quasiparticle eigenstates are Bloch wavefunctions characterized by wavevector  $\vec{k}$  and energy  $\varepsilon$ . As discussed in chapter 2, their dispersion relation,  $\varepsilon(\vec{k})$ , can be measured with momentum resolved techniques such as angle resolved photoemission spectroscopy (ARPES). By contrast, real space imaging techniques, such as scanning tunneling microscopy (STM), cannot be used to measure  $\varepsilon(\vec{k})$ . This is because the local density of states LDOS( $E$ ) spectrum at a single location  $\vec{r}$  is related to the  $\vec{k}$ -space eigenstates  $\Psi_k(\vec{r})$  by

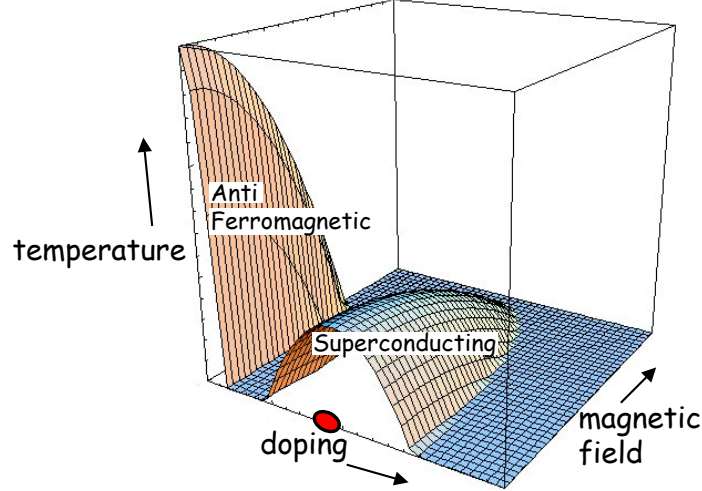


Figure 3.1: A schematic phase diagram of  $\text{Bi}_2\text{Sr}_2\text{CaCu}_2\text{O}_{8+\delta}$ . The red circle shows the area in phase space covered in this chapter. Optimally doped samples are studied at  $T = 4.2$  K, with  $B = 0$  Tesla.

$$\text{LDOS}(E, \vec{r}) \propto \sum_k |\Psi_k(\vec{r})|^2 \delta(E - \varepsilon(\vec{k})) \quad (3.1)$$

Substitution of a Bloch wavefunction into Eqn. 3.1 shows  $\text{LDOS}(E)$  to be spatially uniform.

Sources of disorder such as impurities or crystal defects cause elastic scattering which mixes eigenstates of different  $\vec{k}$  but the same  $\varepsilon(\vec{k})$ . In other words, elastic scattering mixes states that are located on the same quasiparticle contour of constant energy (CCE) in  $\vec{k}$ -space. When scattering mixes states  $\vec{k}_1$  and  $\vec{k}_2$ , the result is a standing wave in the quasiparticle wavefunction  $\Psi_k$  of wavevector  $\vec{q}_{\text{wfn}} = (\vec{k}_1 - \vec{k}_2)/2$ . Since LDOS is proportional to the norm of the quasiparticle wavefunction  $|\Psi_k|^2$ , the LDOS will contain an interference pattern with wavevector  $\vec{q} = \vec{k}_1 - \vec{k}_2$ , or wavelength  $\lambda = 2\pi/q$ . LDOS modulations can be observed by STM as spatial modulations of the differential tunneling conductance  $dI/dV$ .

The Bogoliubov quasiparticles in a BCS superconductor are also Bloch states, but with dispersion

$$E_{\pm}(\vec{k}) = \pm \sqrt{\varepsilon(\vec{k})^2 + \Delta(\vec{k})^2} \quad (3.2)$$

where  $|\Delta(\vec{k})|$  is the  $\vec{k}$ -dependent magnitude of the energy gap at the Fermi surface (CCE for  $\varepsilon(\vec{k}) = 0$  in the normal state). Elastic scattering of Bogoliubov quasiparticles can also

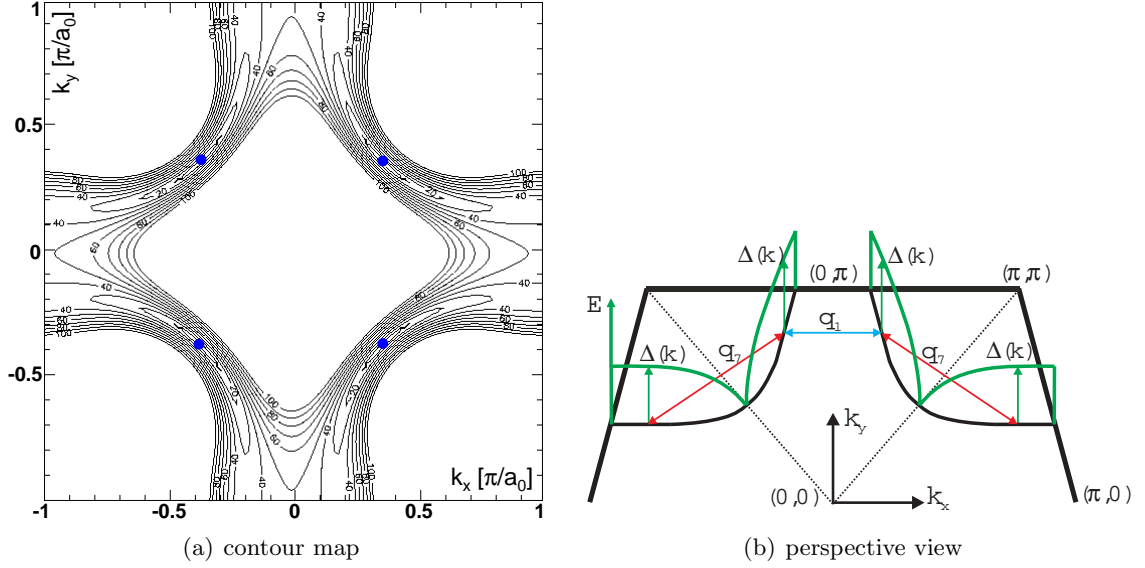


Figure 3.2: Brillouin zone schematic. (a) Contour map of the energy landscape in the first Brillouin zone of BSCCO in the superconducting state. At the four gap nodes (shown in blue), quasiparticle states exist down to zero energy while, at other  $\vec{k}_{FS}$ , a quasiparticle energy  $E = |\Delta(\vec{k}_{FS})|$  is required to create the first excitation. (b) A perspective view of half the first Brillouin zone. The superconducting energy gap  $|\Delta(\vec{k}_{FS})|$  (green) is shown as a function of the location  $\vec{k}_{FS}$  along the normal state Fermi surface (black). Vectors connecting areas of the normal state Fermi surface with identical  $|\Delta|$  are shown and labeled by blue and red arrows depending on the type of elastic scattering process at  $E = |\Delta|$  that connects them.

result in conductance modulations. The trick we employ is to measure the wavelengths of the conductance modulations as a function of energy, and use the  $\vec{k}$ -space symmetries of the band structure (as determined by ARPES) to work backwards to a quantitative map of certain CCE in  $\vec{k}$ -space.

At low temperatures in BSCCO, a  $\vec{k}$ -dependent energy gap  $\Delta(\vec{k})$  opens on the Fermi surface and new quasiparticles appear. As discussed in chapter 2, both the Fermi surface location in momentum-space,  $\vec{k}_{FS}$ , and its energy gap at these locations,  $|\Delta(\vec{k}_{FS})|$ , have been comprehensively studied by ARPES. In Fig. 3.2, we reproduce the superconducting energy landscape in  $\vec{k}$ -space as a contour map, and also as a perspective map with energy along the  $z$ -axis. The latter view perhaps makes it more clear that the energy gap rises from 0 meV at the four nodal points up to a maximum at the edges of the Brillouin zone.

### 3.1.1 Octet Model

A glance at figure 3.2(a) shows that the CCE are complicated. If there is elastic scattering from every point on a given CCE to every other point, there will be density of states modulations of all wavevectors; these will be impossible to untangle. But it turns out that the elastic scattering is dominated by just a few wavevectors.

In a simple metal, the amplitude of scattering obeys Fermi's golden rule:

$$w(i \rightarrow f) \propto \frac{2\pi}{\hbar} |V(\vec{q})|^2 n_i(E_i, \vec{k}_i) n_f(E_f, \vec{k}_f) \quad (3.3)$$

where  $E_i = E_f$  for elastic scattering,  $\vec{q} = \vec{k}_f - \vec{k}_i$ , and  $V(\vec{q})$  is the Fourier component of the scattering potential at wavevector  $\vec{q}$ . For simplicity, we will start with the assumption that  $V(\vec{q})$  is relatively flat in  $\vec{q}$ .

In a superconductor there is an additional complication from coherence factors:<sup>73</sup>

$$w(i \rightarrow f) \propto \frac{2\pi}{\hbar} (u_{k_i} u_{k_f} \pm v_{k_i} v_{k_f}) |V(\vec{q})|^2 n_i(E_i, \vec{k}_i) n_f(E_f, \vec{k}_f) \quad (3.4)$$

where the minus sign is for non-magnetic scatterers, the plus sign is for magnetic scatterers, and  $u_k$  and  $v_k$  for a  $d$ -wave superconductor are given by:

$$v_k^2 = \frac{1}{2} \left[ 1 - \frac{\varepsilon_{\mathbf{k}}}{\sqrt{\Delta_k^2 + \varepsilon_k^2}} \right]; \quad u_k^2 = 1 - v_k^2 \quad (3.5)$$

It is apparent from equations 3.3 and 3.4 that a particular wavevector  $\vec{q}$  can dominate the quasiparticle interference at energy  $E$ , if the  $\vec{k}$ -pairs on the CCE connected by  $\vec{q}$  have a large joint density of states (joint-DOS). So we need to ask, for a given energy  $E$ , which locations in the Brillouin zone have the largest DOS for that energy? The density of states is given by:

$$\text{DOS}(E) = n(E) \propto \frac{1}{|\nabla_k(E)|} \quad (3.6)$$

Therefore, the largest DOS will occur where the gradient  $|\nabla_k(E)|$  is smallest, i.e. where the contours are farthest apart. Because the Brillouin zone has 4 axes of reflection, there will be 8 equivalent locations of highest DOS for a given non-zero energy  $E$ . These locations will be at the end of the "banana"-shaped contours, as shown in figure 3.3. The highest joint-DOS

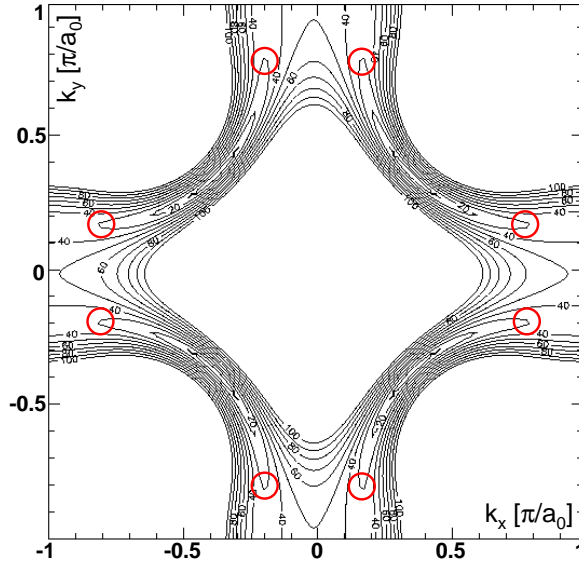


Figure 3.3: Contours of constant energy up to 100 meV in the first Brillouin zone of BSCCO in the superconducting state. At a given energy, say  $E = 30$  meV, the largest contribution to the DOS will come from the eight points where the slope in this “energy landscape” is shallowest, i.e. from within the eight red circles at the ends of the four 30 meV “banana”-shaped contours.

for quasiparticle scattering at this energy occurs at the  $\vec{q}$ -vectors connecting these eight points. We therefore expect the interference-induced conductance modulations to dominate at these connecting  $\vec{q}$ -vectors.

For a given octet at a given energy, there will be  $8 \times 7 = 56$   $\vec{q}$ -vectors connecting the 8 points, but symmetry reduces the set of unique  $\vec{q}$ -vectors to 32. However, since the  $\vec{q}$ -vector manifests itself in our STM images as a modulation at a given wavelength, we cannot distinguish between  $+\vec{q}$  and  $-\vec{q}$ . This further reduces the number of independent  $\vec{q}$ -vectors we can measure to 16. In fact, because of the 8-fold symmetry of the Brillouin zone, there are theoretically only 6 truly independent vectors, but we can measure some of them several times, rotated by  $90^\circ$ , or flipped across an axis of symmetry, and thus we can make 16 independent measurements. The symmetry of these scattering  $\vec{q}$ -vectors is demonstrated in figure 3.4(a).

### 3.1.2 Dispersion

Figure 3.3 shows the relevant octet of points for energy  $E = 30$  meV, and figure 3.4 shows the expected scattering wavevectors for that energy. But this octet will move as a

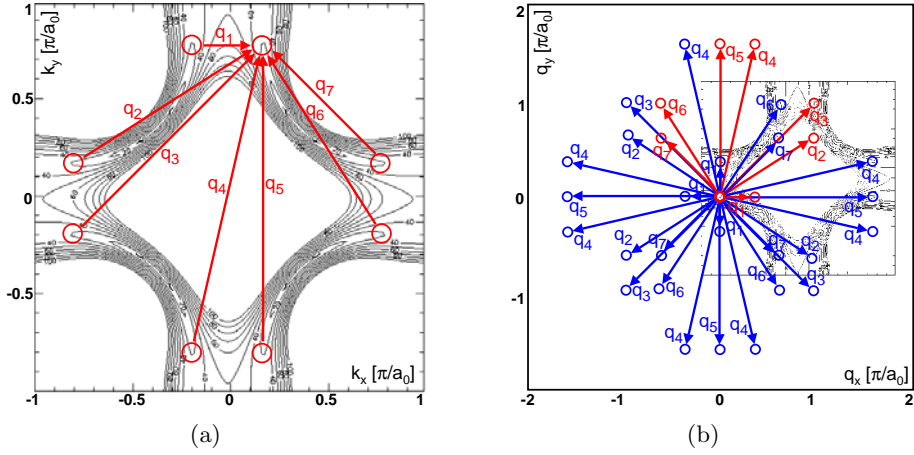


Figure 3.4: Expected scattering wavevectors from octet model. (a) The octet of  $\vec{k}$ -states with highest DOS, and seven labeled  $\vec{q}$ -vectors connecting one point to all its partners. (b) The symmetrized set of  $\vec{q}$ -vectors we would expect to see in a  $\vec{q}$ -space area twice the size of the Brillouin zone. Note that the scale is not the same in (a) and (b): (a) is just the first Brillouin zone, while (b) is two Brillouin zones across.

function of energy; the bananas get longer with increasing energy. For example, we expect  $\vec{q}_1$  to decrease with increasing energy, while we expect  $\vec{q}_7$  to increase with increasing energy. A schematic of the dispersion is shown in figure 3.5.

### 3.1.3 Joint-DOS Calculation

The previous two sections presents the simplest of all possible models: for a given energy we deal with only eight points in  $\vec{k}$ -space. We can make a slightly more complicated (but equally naïve) check by actually calculating the joint-DOS for the whole Brillouin zone, thereby taking into account points that aren't at the ends of the bananas. We can also include the coherence factors, which will tell us which points in  $\vec{q}$ -space may be due to potential or magnetic scattering.

We start with Norman's tight-binding parameterization of the normal state band structure of BSCCO for  $p = 0.17$  hole doping.<sup>74</sup>

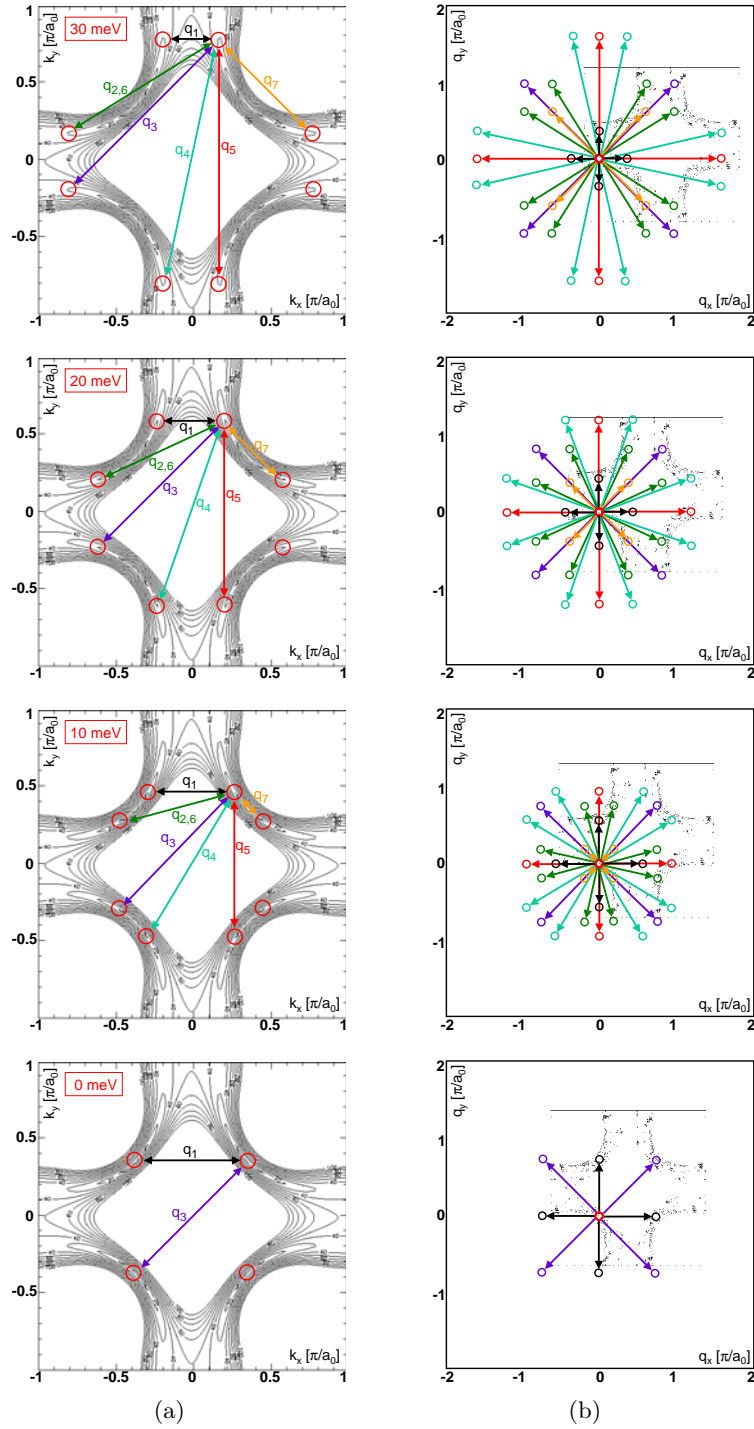


Figure 3.5: Column (a): The octet of  $\vec{k}$ -states with highest DOS, at 4 different energies, with a representative set of  $\vec{q}$ -vectors connecting them. Column (b): The full symmetrized set of 32  $\vec{q}$ -states we would expect to see at the corresponding energies. Note the scale difference between column (a) and column (b).

$$\begin{aligned}
\varepsilon(\vec{k}) = & t_0 \\
& + t_1 * [\cos(k_x) + \cos(k_y)]/2 \\
& + t_2 * \cos(k_x) \cos(k_y) \\
& + t_3 * [\cos(2k_x) + \cos(2k_y)]/2 \\
& + t_4 * [\cos(2k_x) \cos(k_y) + \cos(k_x) \cos(2k_y)]/2 \\
& + t_5 * \cos(2k_x) \cos(2k_y)
\end{aligned} \tag{3.7}$$

where the  $t_i$  are given in table 3.1. (Note that this does not include bilayer splitting, because at the time of publication (1995) bilayer splitting had not been observed in BSCCO.)

Norman has given several different BSCCO parameterizations<sup>a</sup> in different papers:

1. Tight-binding fit by Radtke *et al.*<sup>75</sup> to normal state ARPES data from Dessau *et al.*<sup>58</sup> measured in 1993.
2. Tight binding fit by Norman *et al.*<sup>74</sup> to new normal state ARPES data measured in 1995 by Ding *et al.*<sup>80</sup> on an instrument with higher energy resolution. However, it should be noted that this data still did not show any bilayer splitting (which has since been observed,<sup>81</sup> but only in overdoped  $\text{Bi}_2\text{Sr}_2\text{CaCu}_2\text{O}_{8+\delta}$ ) and also the superconducting part of this data showed two nodes in the gap, at  $35^\circ$  and  $55^\circ$ , rather than the single node at  $45^\circ$  which we now know to exist, due to the  $d_{x^2-y^2}$  pairing. Because this was a fit to normal state data, it probably doesn't matter that the gap data was wrong. This parameterization agrees well with data in another paper by Ding *et al.*,<sup>82</sup> which also shows no bilayer splitting.
3. Some modifications were made to these parameters by Norman *et al.*:<sup>83</sup> the energy contours near the anti-nodal points were flattened, and the nodal points were moved away from (0,0) to compensate. These changes were made to investigate the effects of nesting, but they do not necessarily agree with experimental data.
4. Norman has a later paper giving an alternative set of  $t_i$ 's,<sup>84</sup> which is discussed further by Escrig *et al.*<sup>85</sup> These alternative parameters are less appropriate because they

---

<sup>a</sup>Analogous parameters for YBCO have been given in several papers:

1. Norman parameterization by Radtke *et al.*<sup>75</sup> based on Campuzano data from 1993.<sup>76, 77</sup>
  2. More recent experimental results from ARPES.<sup>78</sup>
  3. Calculated results from a slave-boson approach, which include only the terms  $t_0$ ,  $t_1$ , and  $t_2$ .<sup>79</sup>
- Parameters for LSCO have also been given by Radtke *et al.*<sup>75</sup>

| $t_i$ | function                                                    | Radtke<br>1994 | Norman<br>1995 | Norman<br>2000 | Eschrig<br>2000 |
|-------|-------------------------------------------------------------|----------------|----------------|----------------|-----------------|
| $t_0$ | 1                                                           | 0.0607         | 0.1305         | 0.0879         | 0.0989          |
| $t_1$ | $\frac{1}{2} [\cos(k_x) + \cos(k_y)]$                       | -0.525         | -0.5951        | -0.5547        | -0.5908         |
| $t_2$ | $\cos(k_x) \cos(k_y)$                                       | 0.1            | 0.1636         | 0.1327         | 0.0962          |
| $t_3$ | $\frac{1}{2} [\cos(2k_x) + \cos(2k_y)]$                     | 0.0287         | -0.0519        | 0.0132         | -0.1306         |
| $t_4$ | $\frac{1}{2} [\cos(2k_x) \cos(k_y) + \cos(k_x) \cos(2k_y)]$ | -0.175         | -0.1117        | -0.1849        | -0.0507         |
| $t_5$ | $\cos(2k_x) \cos(2k_y)$                                     | 0.0107         | 0.0510         | 0.0265         | 0.0939          |

Table 3.1: Several different parameterizations of the  $\text{Bi}_2\text{Sr}_2\text{CaCu}_2\text{O}_{8+\delta}$  normal state band structure. I will use the second column in all further calculations, which is for a hole doping close to optimally doped of  $p = 17\%$ , which corresponds to an average gap of  $\Delta_0 \sim 36$  meV.

represent a “bare” dispersion without any interactions; the real material would of course be renormalized by interactions. These changes were made so that these theorists could investigate what kind of interactions might restore the parameters to their experimental values.

The most relevant set of  $t_i$ 's is therefore from the second paper<sup>74</sup> and is reproduced in the second column of table 3.1. However, Norman cautions that the normal state peaks as detected by ARPES are quite broad, so “the accuracy of the dispersion may not be completely adequate.” Furthermore, “the dispersion is definitely renormalized in the superconducting state relative to the normal state.”<sup>b</sup>

Note that the column 2 parameterization we are using was a fit to a sample with  $p = 17\%$  doping. This is close to optimally doped. It corresponds to an average gap of 36 meV, so we will use  $\Delta_0 = 36$  meV when we impose a gap on the normal state parameterization.

We can check the doping of the parameterization simply by adding up the area of the hole pocket. The undoped Mott insulator has an exactly half-filled band, so the hole pocket area would be 50% of the total first Brillouin zone area. For a doped crystal band structure, the fractional area of the hole pocket will be  $f > 0.5$ . Then the doping can be defined as  $p \equiv 2 \times (f - 0.5)$ . I have verified that the column 2 parameterization does indeed correspond to  $p = 17\%$  doping. To a reasonable approximation, the parameterization can be adjusted to reflect a different doping level simply by adjusting the parameter  $t_0$  to expand or contract the hole pocket to the correct area.<sup>c</sup>

<sup>b</sup>Norman: private communication, 2002

<sup>c</sup>Norman: private communication, 2002

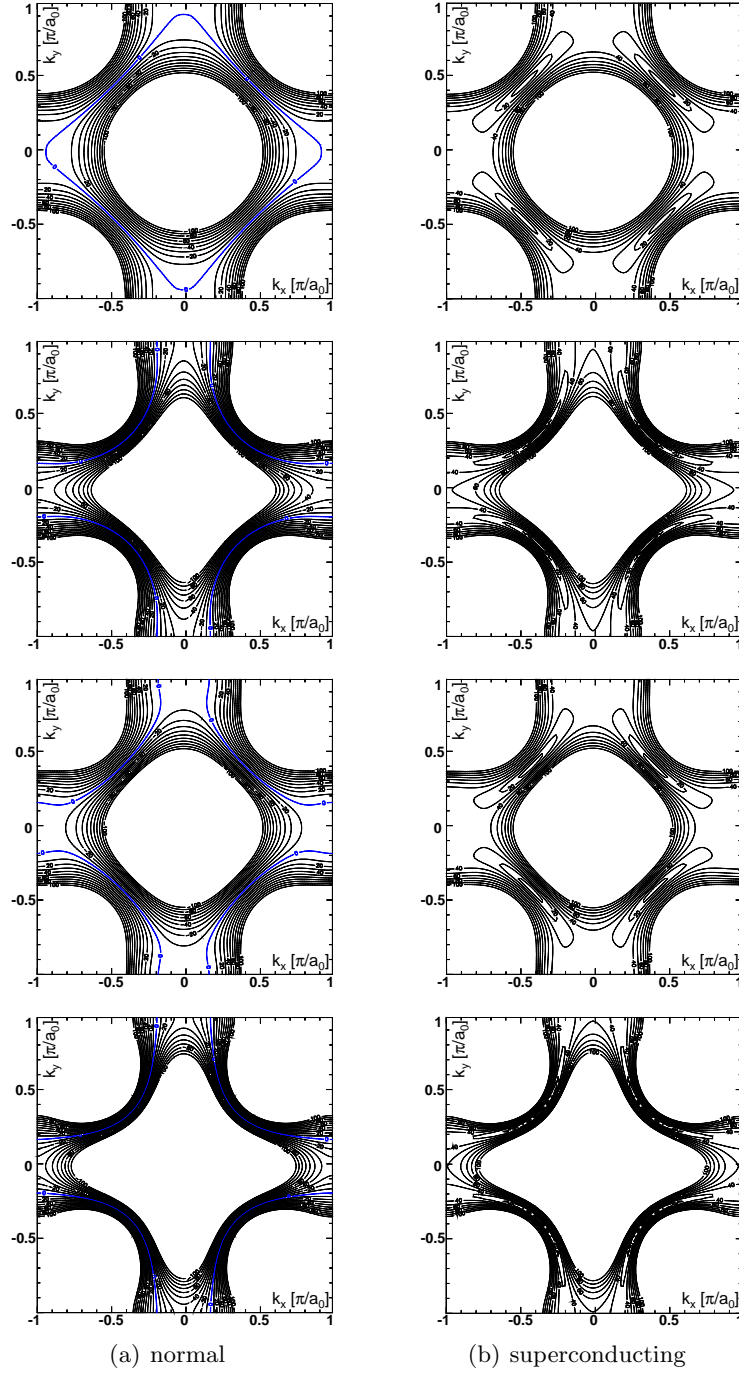


Figure 3.6: Comparison of band structure parameterizations. Column (a) is the normal state and column (b) is the superconducting state. Rows 1–4 in this figure represent columns 3–6 in table 3.1, respectively.

To find the superconducting state band structure, we need a formula for the superconducting gap as a function of angle,  $\Delta_k$ . Several possibilities exist in the literature. Theorists<sup>86</sup> tend to use:

$$\Delta_k = \Delta_0[\cos(k_y) - \cos(k_x)]/2 \quad (3.8)$$

The ARPES community parameterizes the gap as a function of angle from the  $(\pi, \pi)$  point (the  $Y$  point) in the first Brillouin zone. The lowest order terms consistent with  $d_{x^2-y^2}$  symmetry are  $\cos(2\theta)$  and  $\cos(6\theta)$ . Therefore,  $\Delta_k$  can be written as:

$$\Delta_k = \Delta_0[B \cos(2\theta) + (1 - B) \cos(6\theta)] \quad (3.9)$$

where  $B$  is a parameter which depends on doping, according to table 3.2.<sup>63</sup> The comparison between the two methods of gap calculation (and several values of  $B$ ) is shown in figure 3.7.

| doping | $T_c$ | $B$ value                      |
|--------|-------|--------------------------------|
| OD     | 80 K  | 1.0                            |
| OD     | 87 K  | 0.96                           |
| UD     | 83 K  | 0.92                           |
| UD     | 75 K  | 0.89                           |
| UD     | 75 K  | 0.885 (2 <sup>nd</sup> sample) |
| UD     | 80 K  | 0.88                           |

Table 3.2: Mesot parameterization of  $\text{Bi}_2\text{Sr}_2\text{CaCu}_2\text{O}_{8+\delta}$  superconducting gap  $\Delta_k$ .<sup>63</sup>

We can perform another check on the validity of Norman's parameterization by comparing directly to our own data. After imposing the superconducting gap, we can integrate the density of states from Norman's entire first Brillouin zone. We should arrive at a spectrum very similar to that observed via STM with a 36 meV gap. The actual comparison is shown in figure 3.8.

We can also include the coherence factors  $u_k$  and  $v_k$ . Again, there are several different sign and phase conventions for parameterizing these. I use the sign convention according to equation 3.35 in Tinkham.<sup>73</sup>

$$v_k^2 = \frac{1}{2} \left[ 1 - \frac{\varepsilon_{\mathbf{k}}}{\sqrt{\Delta_k^2 + \varepsilon_k^2}} \right]; \quad u_k^2 = 1 - v_k^2 \quad (3.10)$$

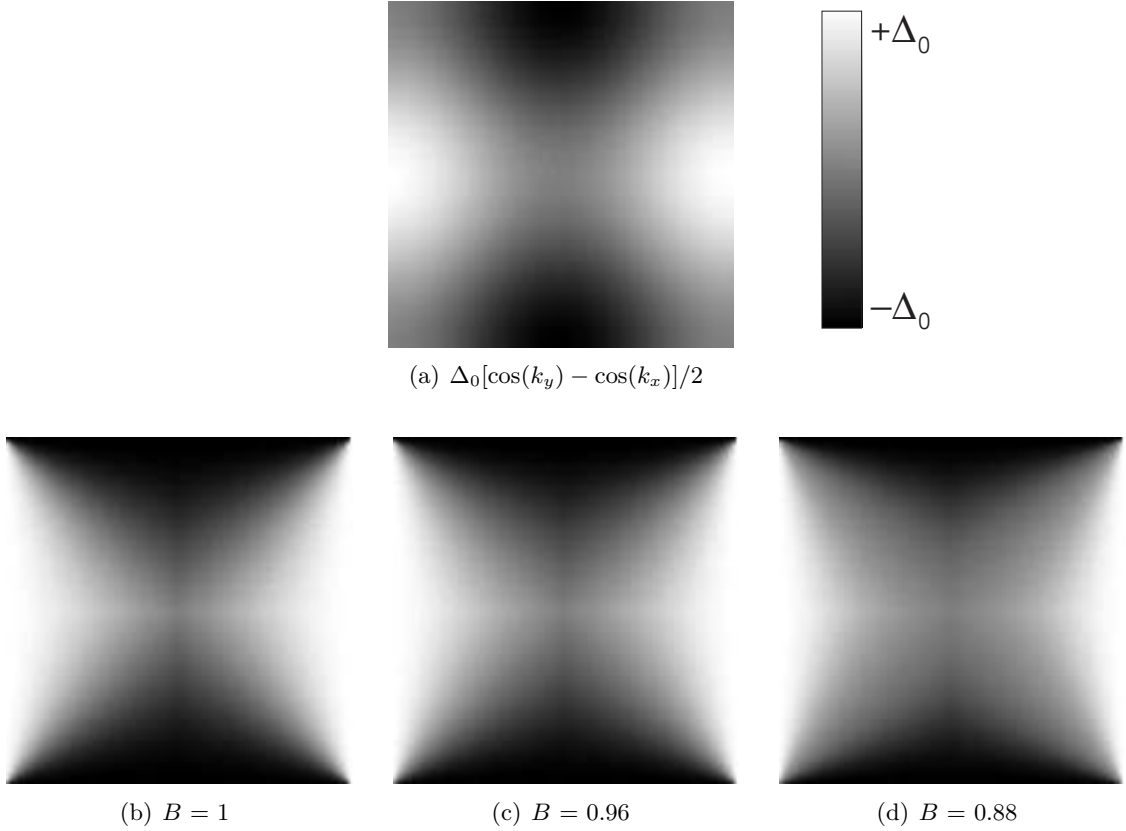


Figure 3.7: Comparison of several possible parameterizations of a  $d$ -wave superconducting gap. (a) Theorist version of a  $d$ -wave gap, calculated using eqn 3.8. Experimentalist version of a  $d$ -wave gap, with (b)  $B = 1$ , (c)  $B = 0.96$ , and (d)  $B = 0.88$ . From this point forward, for our calculations, we will use the gap shown in 3.7(a).

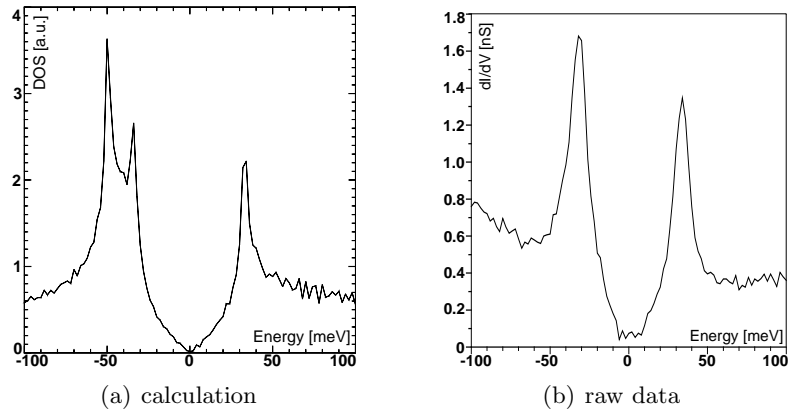


Figure 3.8: Density of states comparison: (a) calculation by numerical integration over Norman's tight-binding band structure parameterization vs. (b) typical STM spectrum on the surface of BSCCO (raw data).

These parameterizations of  $u_k$  and  $v_k$  are shown in figure 3.9.

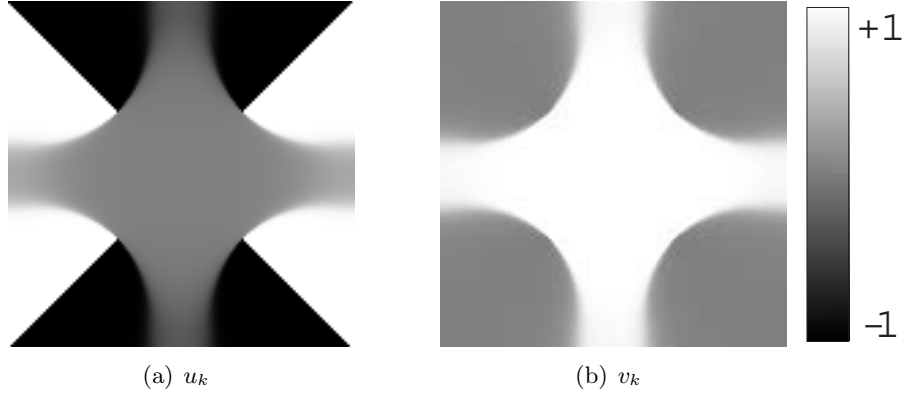


Figure 3.9: (a)  $u_k$  and (b)  $v_k$  for a  $d_{x^2-y^2}$ -wave superconductor, according to Tinkham<sup>73</sup> and equation 3.8.

Finally, having decided all our conventions, we may begin the calculation. The joint-DOS was calculated on a  $512 \times 512$  pixel array, using the normal state band structure parameterization given in column 2 of table 3.1, with gap given by equation 3.8 and  $\Delta_0 = 36$  meV. The basic plan is for each energy, to make a 3-dimensional “histogram” of all allowed scattering  $\vec{q}$ s. In other words, for each pair of states at  $\vec{k}_1$  and  $\vec{k}_2$  which can elastically scatter, we will add one to the 3-dimensional histogram at energy  $\varepsilon(\vec{k}_1) = \varepsilon(\vec{k}_2)$  and location  $\vec{q} = \vec{k}_1 - \vec{k}_2$ .

The experiment was performed at temperature  $T = 4.2$  K which gives an energy broadening of  $\sim 4k_B T = 1.44$  meV. (One factor of 2, because the Fermi function step function is smeared by approximately  $k_B T$  on either side of  $\varepsilon_F$ , and the other factor of 2 because we have thermal broadening in both the initial and final states.) So in the calculation, I allow  $\vec{k}$ -states to “elastically” scatter to other  $\vec{k}$ -states whose energy would differ by up to 1.44 meV in the zero temperature band structure. For example, if  $\varepsilon(\vec{k}_1) = 10$  meV and  $\varepsilon(\vec{k}_2) = 11.44$  meV, I include  $\vec{q} = \vec{k}_2 - \vec{k}_1$  in the count of the scattering wavevectors.

The experiment was performed with a bias voltage modulation of 2 mV RMS, or 5.6 mV peak-to-peak. But energy maps were taken with a 2 meV spacing. So for each pair of states  $\vec{k}_1$  and  $\vec{k}_2$  which can “elastically” scatter (subject to finite temperature broadening), I add one to the histogram in each energy layer within 2.8 meV of  $\varepsilon(\vec{k}_1)$  or  $\varepsilon(\vec{k}_2)$ . In other words, some scattering  $\vec{q}$ s are double-counted in several energy layers, which simulates the real experimental conditions.

For the simplest joint-DOS calculation, I ignore the coherence factors  $u_k$  and  $v_k$ , and simply add one to the histogram at the appropriate energy and  $\vec{q}$  for each allowed pair  $\vec{k}_1$

and  $\vec{k}_2$ . These results are shown in column (a) of figure 3.10. These results confirm visually that the joint-DOS is actually dominated by the banana octet.

The algorithm used was:

```

compute the normal state energy contour map in a 256 x 256 pixel array
impose the superconducting gap
compute the 256 x 256 pixel u_k and v_k arrays
allocate 3 different 512 x 512 pixel x nEnergies arrays
  to hold the results of the plain joint-DOS,
  potential scattering, and magnetic scattering

for each point k1 in the Brillouin zone {
  for each point k2 in the Brillouin zone {
    if ( |e(k1)-e(k2)| < 4 k_B T ) then {
      q = k1 - k2
      for each energy E {
        if |E - ( e(k1)+e(k2) )/2| < 4 k_B T + e dV {
          add 1 to jdos(E)
          add u_k1 * u_k2 + v_k1 * v_k2 to mag(E)
          add u_k1 * u_k2 - v_k1 * v_k2 to pot(E)
        }
      }
    }
  }
}

```

Note that realistic parameter choices are essential to arriving at this result. First, if we don't use a high enough resolution  $x \times y$  grid, we arrive at confusing results. The real material, of course, has a grid of infinite resolution. [Note that our STM measurements sample at finite resolution, but the interference patterns themselves do have infinite resolution.] So our  $512 \times 512$  pixel grid comes closest to approximating the real situation. Results from smaller grids are shown in figure 3.11. Secondly, if we don't use realistic energy broadening parameters, we arrive at confusing results. The real material is sitting at  $T = 4.2$  K, so there really will be some "elastic" scattering between  $\vec{k}$  locations whose energies differ slightly. And the real experiment does include  $\vec{q}$  states from a finite energy range in each map, even overlapping with the map at nearest energy. Results from unrealistically small energy broadening parameters are shown in figure 3.12.

One interesting aspect of this calculation is that the most naïve joint DOS calculation shows 16 distinct peaks in  $\vec{q}$ -space, while magnetic and scalar scattering each show a complementary set of 8  $\vec{q}$ -peaks. In the real experiment, we see all 16 peaks, which suggests that we have multiple types of scattering present in the crystal.

However, we caution that even this calculation is exceedingly naïve. We are effectively taking into account only the imaginary part of the Green's function. A full scattering model

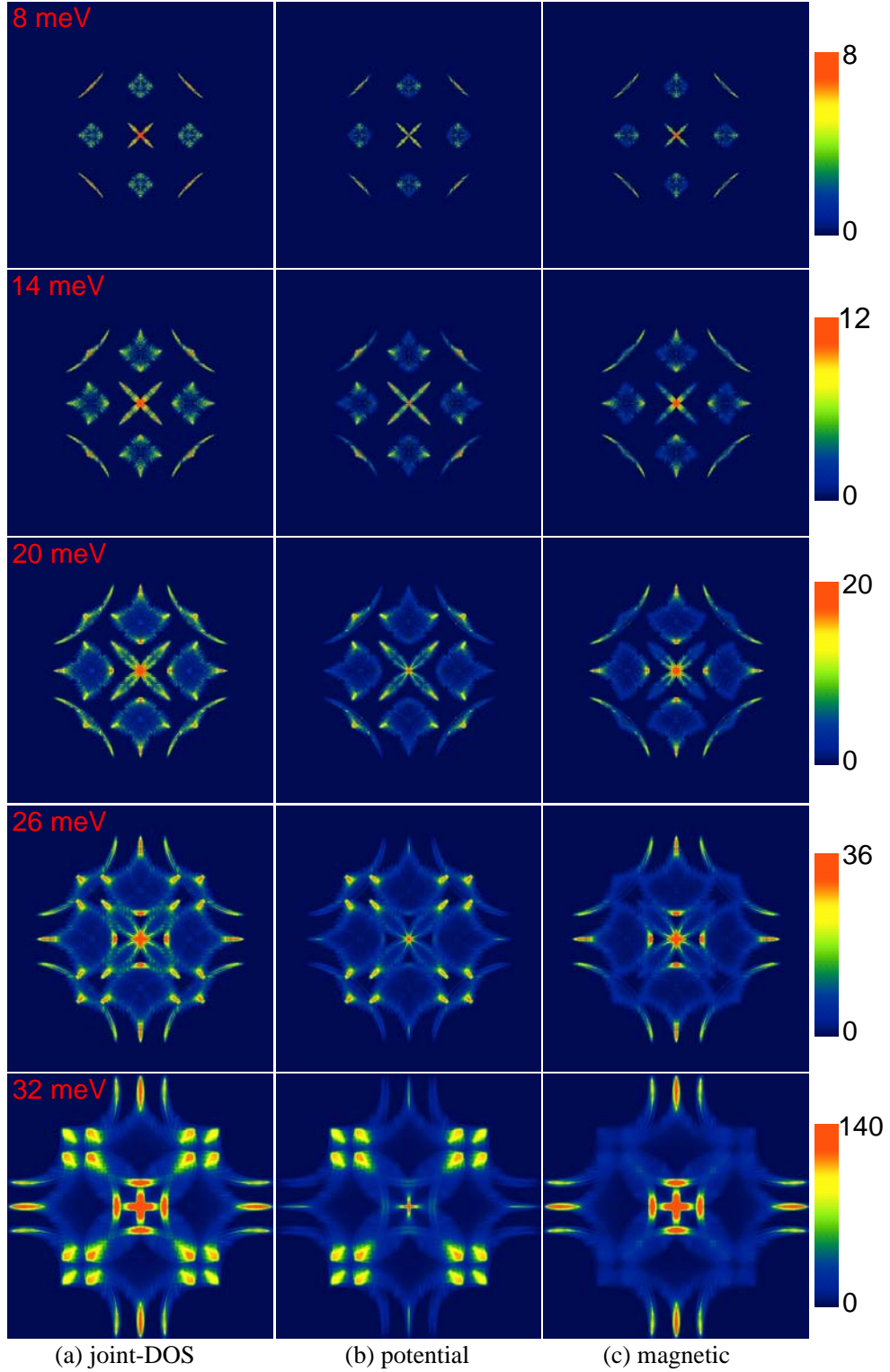


Figure 3.10: The results of a joint-DOS calculation on the full Brillouin zone, with (a) no coherence factor; (b) coherence factor  $(u_{k_i}u_{k_f} - v_{k_i}v_{k_f})$  for potential scatterers; and (c) coherence factor  $(u_{k_i}u_{k_f} + v_{k_i}v_{k_f})$  for magnetic scatterers. Scalebars show arbitrary units, which are however consistent from one energy to the next.

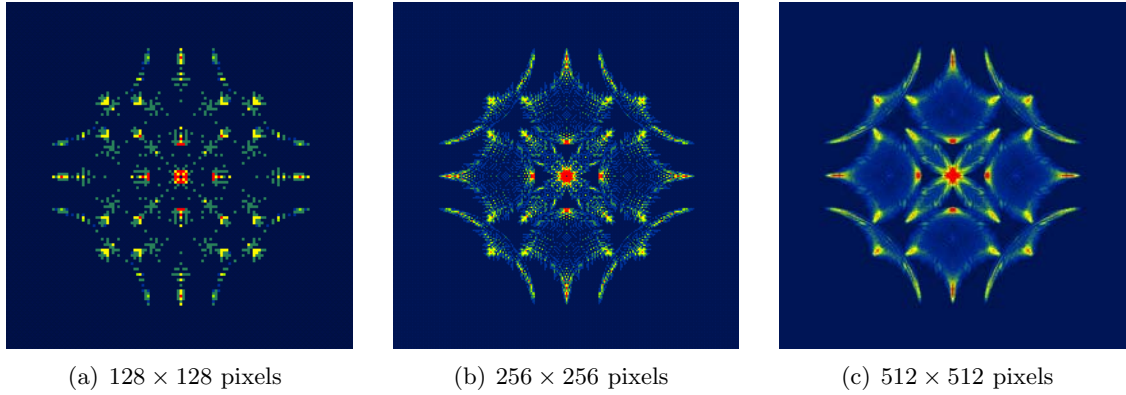


Figure 3.11: Comparison between joint-DOS calculations with different pixel resolution, at  $E = 24$  meV. If the calculation is performed with insufficient pixel resolution, as in (a), the dominant scattering vectors do not stand out as strongly against the background, as they do when the calculation is performed at higher spatial resolution, as in (c).

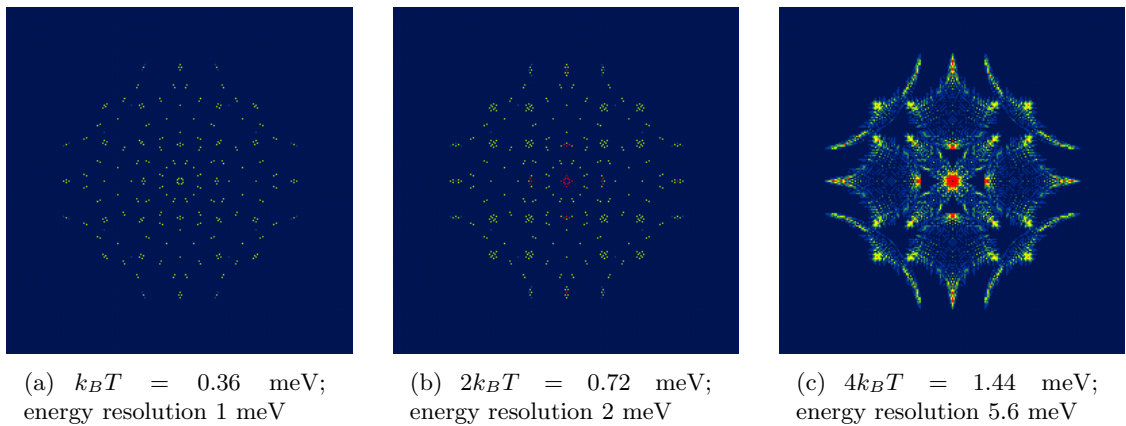


Figure 3.12: Comparison of joint-DOS calculations at  $E = 24$  meV with different energy broadening. Both thermal broadening and experimental energy resolution increase from (a) to (c). Results in (a) and (b) may be misleading, whereas the broadening parameters and resulting joint-DOS in (c) most closely approximate the real crystal.

would include also the real part of the Green's function, which leads to the appearance of other points in  $\vec{q}$ -space.<sup>86</sup>

## 3.2 Data

I will show here the results of high-resolution LDOS imaging at 4.2 K on BSCCO crystals grown by the floating zone method with superconducting transition temperature ranging between underdoped ( $T_c = 78$  K) and slightly overdoped ( $T_c = 85$  K). The samples are cleaved at the BiO plane in cryogenic ultra high vacuum and immediately inserted into the STM head. Atomic resolution is achieved throughout the studies reported here. On these surfaces, we acquire maps of the differential tunneling conductance ( $g = dI/dV$ ) measured at all locations  $(x, y)$  in the field of view. Because  $\text{LDOS}(E = eV) \propto g(V)$ , where  $V$  is the sample bias voltage, this results in a two dimensional map of the LDOS at each energy  $E$ .

Figure 3.13 shows a topographic image and three LDOS maps for quasiparticle energies centered at 12, 16, and 22 meV, all acquired in the same 650 Å field of view with 1.3 Å spatial resolution. Periodic LDOS modulations are evident in all images (although one also sees remnants of impurity scattering at low energies and of gap disorder at high energies). Notably, quite different spatial patterns and wavelengths are observed at each energy.

At low energies, the strongest modulations run along the  $a$  and  $b$  axes. At high energies, the strongest modulations run along the  $x$  and  $y$  axes. At intermediate energies, both orientations are apparent. We expect multiple modulations to be present across all energies, but there is no way they can all be discerned in real space by eye.

### A note on image size & resolution

It is important to choose carefully the data image size and resolution. Ideally, all measurements would be instantaneous, and we would have time to measure an arbitrarily large field of view with arbitrarily fine resolution. But in practice, we are limited by measurement time. Doubling the linear dimension of the image quadruples the time, as does doubling the image resolution. So with a finite amount of time to make a measurement, we must prudently balance the advantages of large images and fine resolution.

A large  $\vec{R}$ -space image leads to fine  $\vec{q}$ -space resolution, while a fine  $\vec{R}$ -space resolution leads to large  $\vec{q}$ -space image. In order to look for weakly dispersing  $\vec{q}$ -vectors, we need  $\vec{q}$ -space resolution  $\sim 1\%$  of the Brillouin zone, which means that our  $\vec{R}$ -space image must have extent at least  $100a_0 = 383$  Å. In order to see all  $\vec{q}$ -vectors, we must have  $\vec{q}$ -space extent

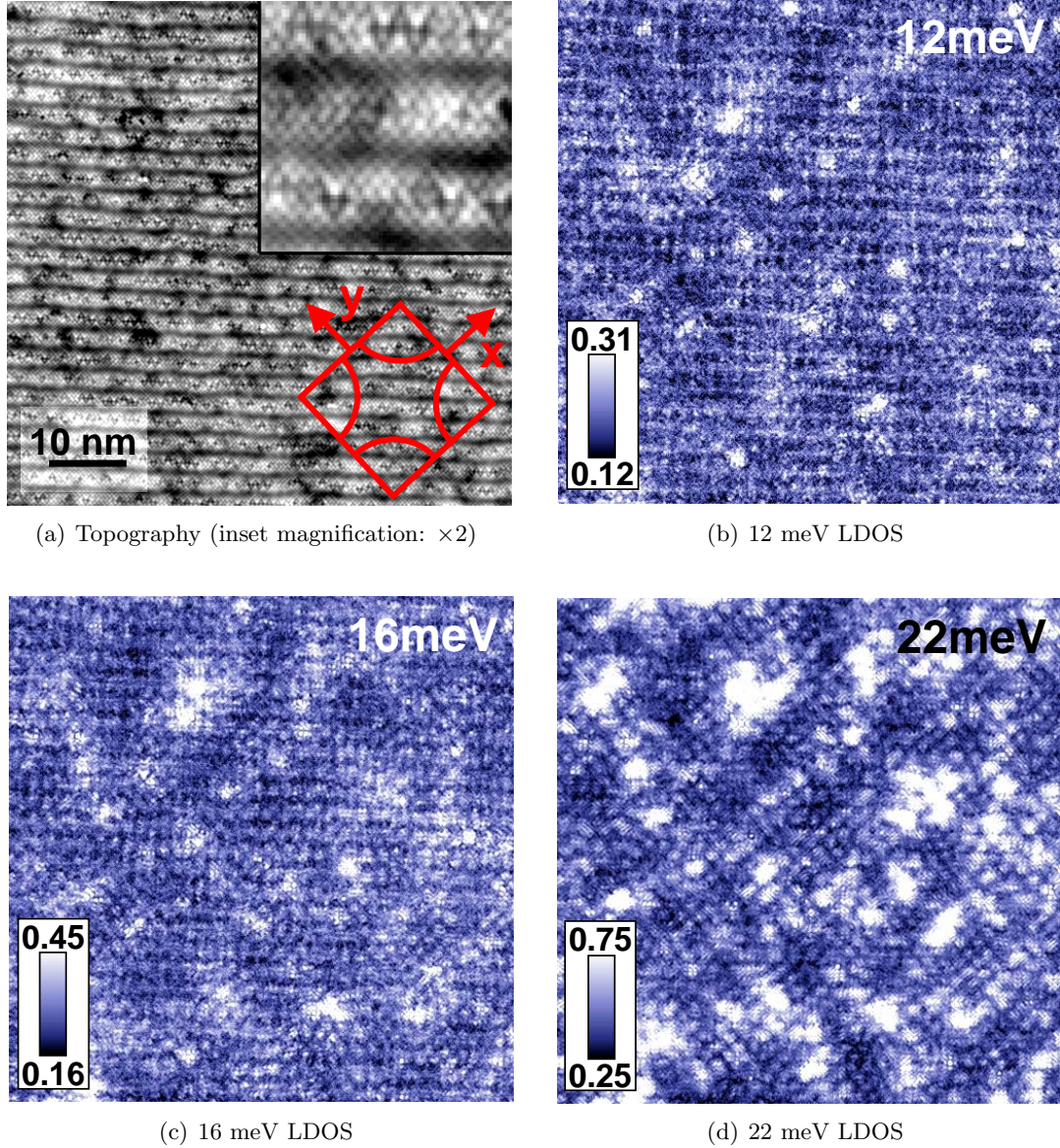


Figure 3.13: Four unprocessed images of a single 650 Å field of view with 1.3 Å resolution. All measurements reported in this paper were obtained at a junction resistance of 1 GΩ set at a bias voltage of -100 mV, so the total junction conductance is  $10^3$  picoSiemens (pS). All LDOS images were acquired with a bias modulation amplitude of 2 mV root mean square. From the atomic resolution in (a) one can see the direction of the Cu-O bonds and the incommensurate supermodulation of wavelength  $\sim 26$  Å at  $45^\circ$  to the bonds. A cartoon showing the relative orientation of the Brillouin zone is superimposed in red. The LDOS images show checkerboard-like modulations of the LDOS: (b)  $45^\circ$  to the Cu-O bonds at  $\vec{q}_7 \sim 0.21(\pm 2\pi/a_0, \pm 2\pi/a_0)$ ; (c) both  $45^\circ$  to and along the Cu-O bonds at  $\vec{q}_7 \sim 0.25(\pm 2\pi/a_0, \pm 2\pi/a_0)$  but also at  $\vec{q}_1 \sim 0.22(0, \pm 2\pi/a_0)$  and  $\vec{q}_1 \sim 0.22(\pm 2\pi/a_0, 0)$ ; (d) along the Cu-O bonds at  $\vec{q}_1 \sim 0.20(0, \pm 2\pi/a_0)$  and  $\vec{q}_1 \sim 0.20(\pm 2\pi/a_0, 0)$ .

at least twice the size of the first Brillouin zone, which means that our  $\vec{R}$ -space resolution must be at least 1 pixel per  $a_0/2 = 1.9 \text{ \AA}$ . This relationship is demonstrated in figure 3.14.

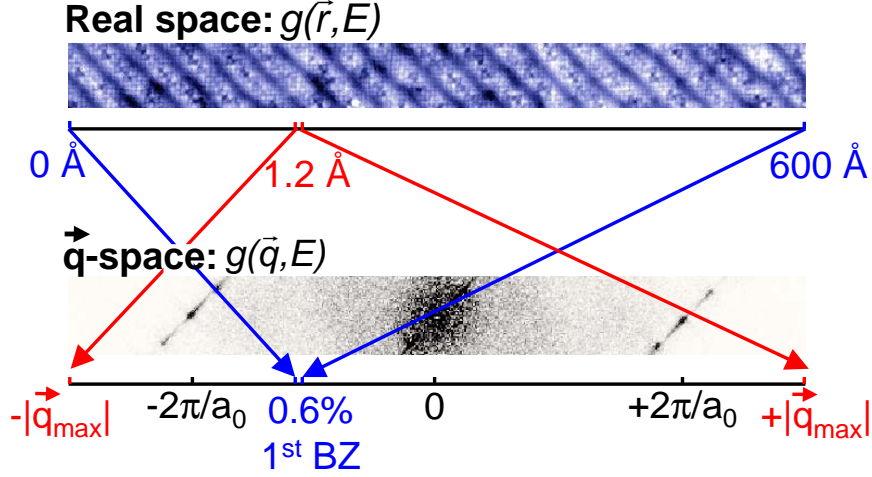


Figure 3.14: Relationship between  $\vec{R}$ -space and  $\vec{q}$ -space resolution. By choosing a  $\vec{R}$ -space image with size  $600 \text{ \AA}$  and resolution 1 pixel per  $1.2 \text{ \AA}$ , we arrive at a  $\vec{q}$ -space image with size 3 Brillouin zones, and resolution  $0.6\%$  of a Brillouin zone.

### 3.3 Analysis

To explore the evolution of all these LDOS modulations with energy, I compute the magnitude of the Fourier transform,  $|\text{FT}(E, \vec{q})|$ , shown in figure 3.15. In Fourier space ( $\vec{q}$ -space) we can clearly visually separate the different coexisting modulations; each appears as a distinct bright spot in the Fourier transform. By comparing these maps with the joint-DOS prediction in figure 3.10, we can already see qualitatively that all the peaks are present and in approximately the correct positions.

In the remainder of this chapter, I will focus on the two inner points  $\vec{q}_1$  and  $\vec{q}_7$ , as labeled in figure 3.4. First,  $\vec{q}_1$  is oriented toward the  $(\pm\pi, 0)$  and  $(0, \pm\pi)$  direction. It appears at finite  $|\vec{q}|$  at very low energy and then moves steadily inwards towards  $(0, 0)$  (i.e.  $|\vec{q}_1|$  decreases as  $E$  increases). Second,  $\vec{q}_7$  is oriented along the  $(\pm\pi, \pm\pi)$  direction. It appears and moves steadily to larger  $|\vec{q}|$  with increasing energy (i.e.  $|\vec{q}_7|$  increases as  $E$  increases). These same phenomena associated with  $\vec{q}_1$  and  $\vec{q}_7$  have been observed for all eight samples we have studied in this manner, but the exact dispersion of the peaks varies systematically with doping.

In figure 3.16, I plot the measured value of  $|\text{FT}(E, \vec{q})|$  versus  $|\vec{q}|$  along the  $(\pi, 0)$  and

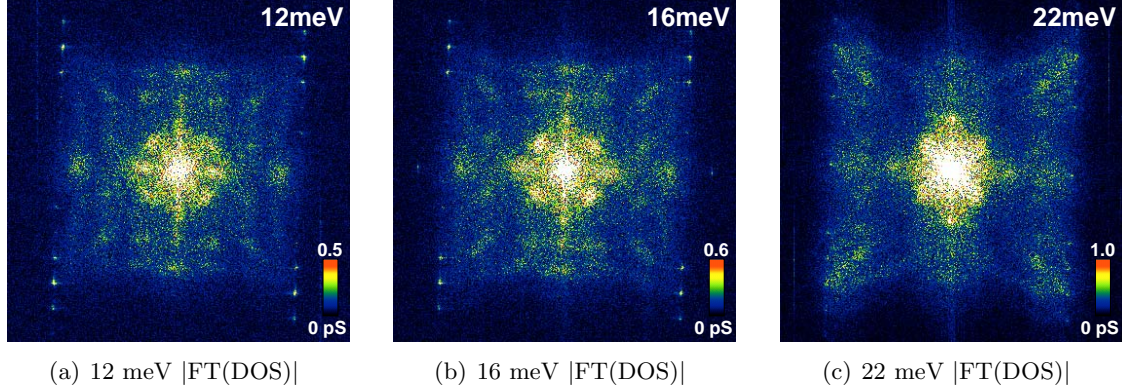


Figure 3.15: Fourier transforms of the 3 LDOS images shown in figure 3.13. The local maxima in these images represent the dominant  $\vec{q}$ 's associated with quasiparticle scattering at each energy  $E$ . The innermost scattering wavevectors oriented parallel to  $(\pm\pi, 0)$  and  $(0, \pm\pi)$  become shorter as energy rises. In contrast, the innermost scattering wavevectors oriented parallel to  $(\pm\pi, \pm\pi)$  become longer as energy rises. The harmonics of the supermodulation are sharp features observed at the same location in all  $\text{FT}(E, \vec{q})$  images.

$(\pi, \pi)$  directions, at several energies, for an underdoped sample with  $\bar{\Delta} = 50.2$  meV. These cuts pass directly through peaks  $\vec{q}_1$  and  $\vec{q}_7$ , respectively. The locations of the  $|\text{FT}(E, \vec{q})|$  peaks are measured by fitting an exponential decay plus a Lorentzian. The dispersion in the unprocessed data is obvious. In figure 3.17, I show the energy dependence of the peaks in  $\text{FT}(E, \vec{q})$  for  $\vec{q}$ -vectors oriented toward the  $(\pi, 0)$  direction [ $\vec{q}_1(E)$ ], and towards the  $(\pi, \pi)$  direction [ $\vec{q}_7(E)$ ]. The dispersions of these two types of conductance modulations were analyzed in detail for data for three of the samples. One is underdoped with mean energy gap value  $\bar{\Delta} = 50.2$  meV (red squares), the second is near optimal with  $\bar{\Delta} = 43.7$  meV (green circles), and the third is slightly overdoped with  $\bar{\Delta} = 36.7$  meV (blue triangles). In general, one can see that at fixed  $E$ ,  $\vec{q}_1(E)$  becomes shorter, whereas  $\vec{q}_7(E)$  becomes longer, as the doping is increased.

Now we compare our  $\vec{q}$ -space data quantitatively with the directly measured ARPES  $\vec{k}$ -space data. Consider first the  $\vec{q}_1$  data from the  $(\pi, 0)$  direction, which corresponds to the blue arrow in figure 3.2(b). These wavevectors are parallel to  $(0, \pm\pi)$  or  $(\pm\pi, 0)$  but have different  $|\vec{q}_1|$  depending on the value of  $\Delta$  at the points being connected. We estimate the expected  $\vec{q}_1(\Delta)$  in our model using ARPES measurements of  $|\Delta(\vec{k})|$  and locations of  $\vec{k}_{FS}$ .<sup>57</sup> The result is shown as grey bands in figure 3.17(a). The ARPES-derived results and our measured  $\vec{q}_1$  are in excellent quantitative agreement. With increasing doping, the measured range of  $\vec{q}_1$  becomes systematically shorter, as shown in figure 3.17(a). This would

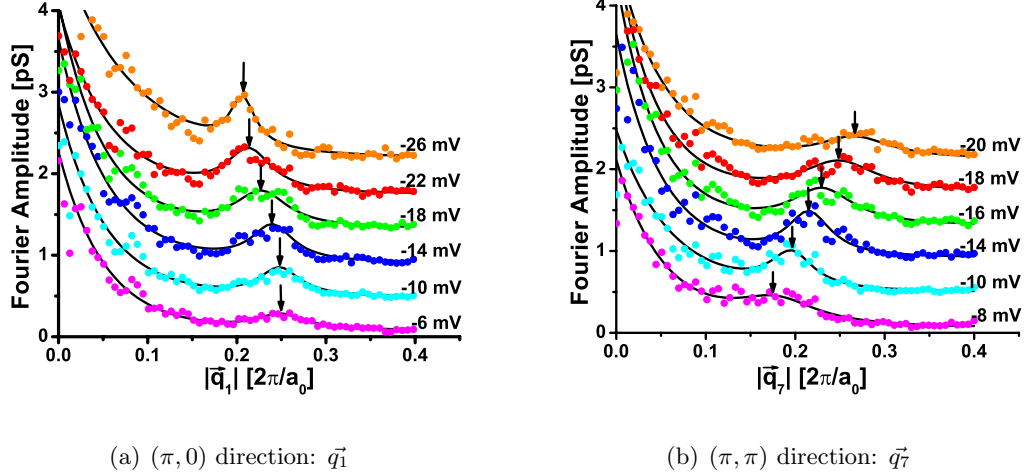


Figure 3.16: The amplitude of  $\text{FT}(E, \vec{q})$  versus  $|\vec{q}|$  along (a) the  $(\pi, 0)$  direction and (b) the  $(\pi, \pi)$  direction are shown for six quasiparticle energies. The data are shifted vertically relative to each other by 0.4 pS for clarity. Each solid black line is a fit to an exponential decay from  $\vec{q} = 0$  plus a Lorentzian peak. An arrow points to the local maximum in  $|\vec{q}|$  for each energy.

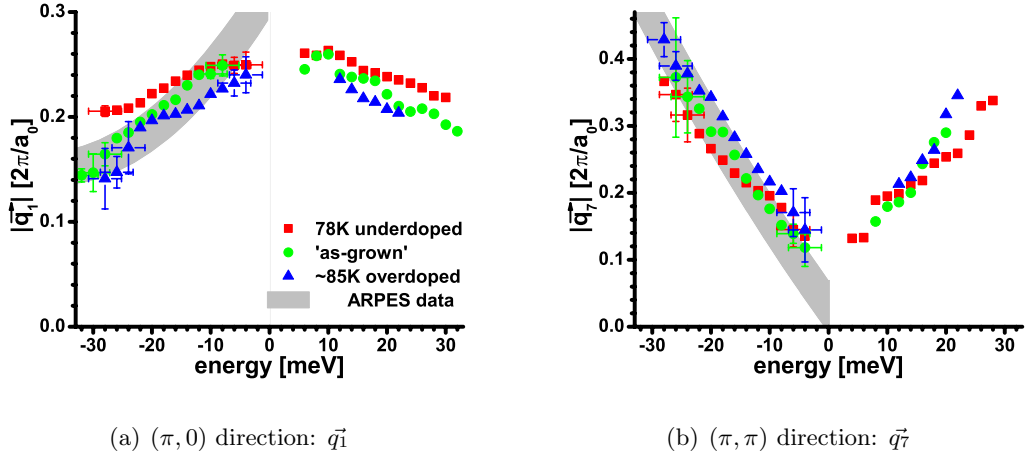


Figure 3.17: The measured  $\vec{q}(E)$  for (a) the  $(\pi, 0)$  direction and (b) the  $(\pi, \pi)$  direction are plotted for samples of three different dopings. The error bars shown at the end of the data ranges are representative of the uncertainty in identifying the location due to the peak width. The shaded grey bands represent the expected dependence  $\vec{q}(E)$  derived from ARPES using the model described in the text. Note that ARPES measures only the electron-like portion of the spectrum. The width of the band represents uncertainties in the published ARPES data. These ARPES data from a  $T_c = 87$  K Bi-2212 sample<sup>57</sup> should be compared with data from our similarly doped sample (green circles), which are in excellent agreement with the simplified model.

be expected if increased hole density expands the hole pocket and moves the almost-parallel sections of the Fermi surface closer together.

Now consider the  $\vec{q}_7$  data from the  $(\pi, \pi)$  direction, which corresponds to the red arrow in figure 3.2(b). The  $\vec{q}_7$  peaks evolve very differently with energy than those oriented toward  $(\pi, 0)$ . Their dispersion has opposite sign and is substantially faster. We consider scattering that connects the same range of  $\vec{k}$ -states on the Fermi surface as for the  $(\pi, 0)$ -oriented process, but now diagonally across the inside of the hole pocket by the vector  $\vec{q}_7$  parallel to  $(\pi, \pi)$  (Fig. 1, red arrows). We can again estimate the expected  $|\vec{q}_7(\Delta)|$  using ARPES data.<sup>57</sup> The result is shown as a grey band in figure 3.17(b). The ARPES-derived results and our measured  $\vec{q}_7(E)$  are in excellent quantitative agreement. Furthermore, with increasing doping, the range of  $\vec{q}_7(\Delta)$  moves to higher values, again as expected if increased hole density increases the area of the hole pocket and the distance between relevant sections of the Fermi surface.

### 3.4 Sources of Scattering

#### Does disorder cause the scattering?

There is much evidence from experiments other than STM that quasiparticle scattering is important in BSCCO. For example, THz spectroscopy shows that low-temperature quasiparticle mean free paths in optimal BSCCO are about two orders of magnitude below that of optimal YBCO,<sup>87</sup> indicating that appreciable quasiparticle scattering exists in BSCCO. ARPES also shows a short quasiparticle lifetime for anti-nodal quasiparticles.<sup>88</sup>

With our spatially resolved tools, we ask what is the range of coherent quasiparticle interference patterns and where are the scattering centers? The smallest  $\vec{q}$ -space extent of any  $\text{FT}(E, \vec{q})$  peak in figure 3.16 is  $\Delta q \sim 0.1\pi/a_0$ . This indicates that the longest coherence length for any modulation is  $\ell \sim 80 \text{ \AA}$ . Several phenomena such as Ni and Zn impurity resonances with spacing  $\sim 100 \text{ \AA}$  (visible in figure 3.13), gap disorder with patch size  $\sim 30 \text{ \AA}$ ,<sup>89, 90, 91, 92</sup> or oxygen atoms with spacing  $\sim 13 \text{ \AA}$  at this nominal doping, may influence this DOS modulation coherence length  $\ell$ .

However, we observe qualitatively the same quasiparticle interference patterns independent of the concentration of Ni or Zn impurities. In fact, we see the quasiparticle interference patterns even in samples with no Ni or Zn impurities. Therefore the Ni and Zn impurities cannot be solely responsible for the quasiparticle interference. All samples have some native point defects, but a direct correlation between the point defects and the quasiparticle

interference has not yet been possible.

We can also conclude from the joint-DOS modeling with coherence factors in figure 3.10 that there are significant sources of both magnetic and potential scattering. The experimental data shows all 16 quasiparticle interference peaks in  $\vec{q}$ -space, while either magnetic or potential scatterers alone would result in only 8  $\vec{q}$ -space peaks.

Furthermore, in all samples there are multiple non-dispersing single-pixel “peaks” in the vicinity of each broader, dispersing  $\vec{q}_i$  peak. Examples of these single-pixel peaks are shown in figure 3.18 for several samples. These non-dispersing single-pixel peaks can be explained as simply the power spectrum of a random impurity distribution, as described in figure 17 of Capriotti *et al.*<sup>93</sup> The fact that these single-pixel peaks do not appear at the same wave-vector from one sample to the next, or in fact even from the  $x$ -axis to the  $y$ -axis within the same sample, suggests that they result from disorder rather than from a more fundamental underlying order of fixed wavevector.

### Does order cause the scattering?

We also consider the possibility that the observed quasiparticle interference patterns are caused primarily by scattering off an underlying charge or “stripe” order of fixed wavevector  $\vec{q}_0$ .<sup>94, 95</sup> According to equation 3.4, reproduced here,

$$w(i \rightarrow f) \propto \frac{2\pi}{\hbar} (u_{k_i} u_{k_f} \pm v_{k_i} v_{k_f}) |V(\vec{q})|^2 n_i(E_i, \vec{k}_i) n_f(E_f, \vec{k}_f),$$

the scattering intensity is a product of the scattering potential  $V(\vec{q})$  and the joint-DOS. If the scattering potential consists solely of an underlying order of single fixed wavevector  $\vec{q}_0$ , then  $V(\vec{q}) = \delta(\vec{q} - \vec{q}_0)$ , so scattering intensity will be non-zero only at  $\vec{q} = \vec{q}_0$ . However, if the underlying order has a short coherence length  $L$ , due to disorder and/or pinning, then the scattering potential  $V(\vec{q})$  will consist of a peak of finite width  $\delta q \sim 1/L$  centered around  $\vec{q}_0$ . The scattering intensity will be enhanced at  $\vec{q} = \vec{q}_0$ , but because of the simultaneous influence of the joint-DOS, the wavevector of maximum scattering intensity may disperse across the range  $\delta q$ .

We can make a few relevant observations as follows. First, in all samples studied, we clearly see 16 dispersing bright spots in  $\vec{q}$ -space. In order to explain this solely as scattering off underlying order of fixed  $\vec{q} = \vec{q}_0$ , we would need 16 different underlying orders with 16 different fixed  $\vec{q}_0$ 's. Furthermore, some of these 16 underlying orders would need a very short coherence length, such that the width  $\delta q$  of the  $V(\vec{q}_0)$  peak could accommodate the

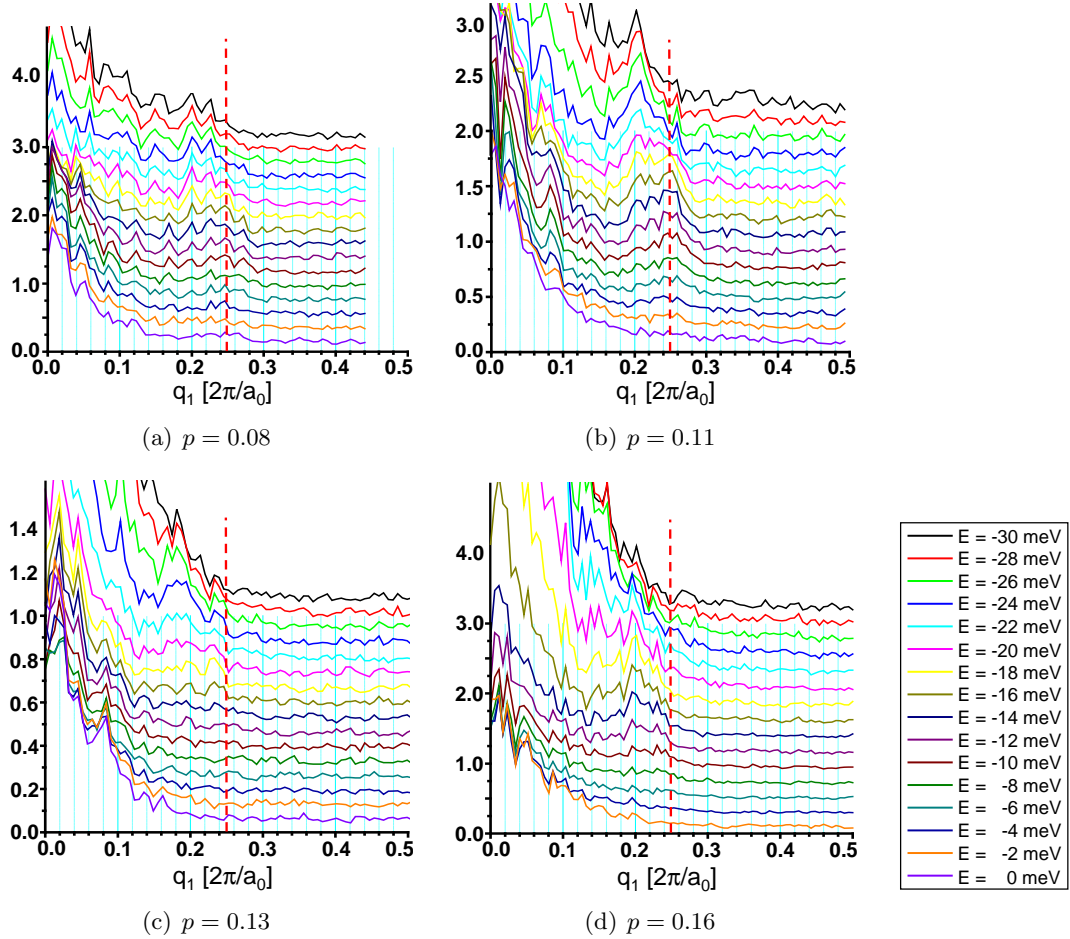


Figure 3.18: Single-pixel, non-dispersing  $\vec{q}$ -space peaks for four different samples. These peaks result from the power spectrum of the particular random impurity distribution in the field of view measured. A red vertical line is shown in each figure at  $\vec{q} = 0.25[2\pi/a_0]$  for reference, to demonstrate that the single-pixel peaks occur at different values of  $\vec{q}$  in each sample.

full dispersion of the joint-DOS wavevectors. The full dispersion is, for some  $\vec{q}_i$ 's, up to 30% of the Brillouin zone, meaning the underlying “order” would actually be disordered on a three unit cell length scale.

If the scattering is based on random disorder plus susceptibility to an underlying order,<sup>95</sup> we would expect a peak in scattering intensity at a specific  $\vec{q}_0$ . The intensity of dispersing  $\vec{q}_i$ 's we observe do peak at certain values. But the peak values appear to vary from one sample to another. For example, the scattering intensity vs. wavevector  $\vec{q}_1$  is shown for three samples of different dopings in figure 3.19.

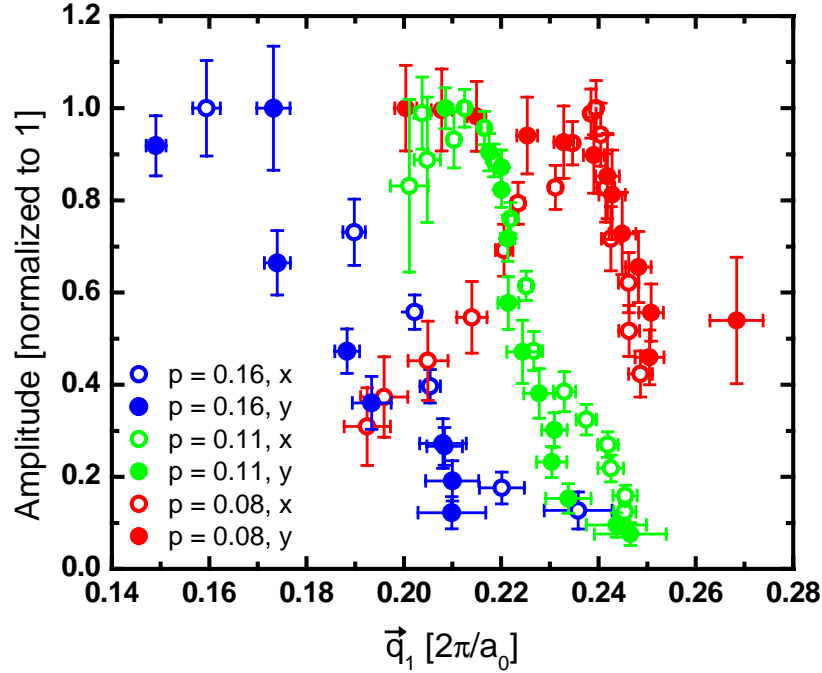


Figure 3.19: Scattering intensity vs. wavevector  $\vec{q}_1$  for three samples of different doping. For each  $dI/dV$  map at each energy  $E$ , the relevant bright spot in  $\vec{q}$ -space was fit to find both the value of  $\vec{q}_1$  and the area  $A$  under the  $\vec{q}_1$  peak. Here the results are plotted as  $A$  vs.  $\vec{q}_1$ . To account for differences in tips, for each axis of each sample, the largest scattering intensity has been normalized to one. The wavevector  $\vec{q}_1$  of maximum scattering intensity  $A$  increases with decreasing doping. This figure is, however, somewhat misleading. In order to extract the maximum susceptibility  $\propto V(\vec{q})$  from the maximum scattering intensity, we would need to divide out by the joint-DOS. Since the joint-DOS increases with increasing energy, and  $\vec{q}_1$  decreases with increasing energy, division by joint-DOS will shift the maximum susceptibility wavevectors to larger values, or shorter wavelengths. A more thorough analysis is needed.

In conclusion, we do not see a single underlying order which has the same fixed wavevector  $\vec{q}_0$  in each sample. Even within a single sample, the dispersing modulations we see cannot be explained wholly in terms of scattering off an underlying ordering of fixed wavevector, unless we postulate 16 underlying orders all coincidentally similar to the 16 wavevectors selected by the joint-DOS analysis. Furthermore, we caution against interpreting non-dispersing, high-intensity single pixels as signs of an underlying order; unless they are repeatable from sample to sample they must be just a remnant of the random disorder in each sample, as demonstrated in here in figure 3.18 and in figure 17 of Capriotti *et al.*<sup>93</sup>

## 3.5 Review of Related Studies

### 3.5.1 Prior STM measurements of Quasiparticle Interference

Although this work represents the first application of FT-STs to the cuprates, I would like to credit similar techniques which have previously been applied to other materials. STM studies of conductance modulations allowed the first direct probes of the quantum interference of electronic eigenstates in metals and semiconductors. Quasiparticle interference was first observed in copper at 4 K<sup>96</sup> then in gold at room temperature<sup>97</sup> due to step edges and impurities. Subsequent experiments on Cu and Ag<sup>98</sup> used a model of Friedel oscillations<sup>99</sup> from a step edge to extract the quasiparticle lifetimes from the spatial decay length of the interference patterns. An experiment on sub-surface impurities in the semiconductor InAs used the energy dependence of the interference patterns surrounding the impurities to find the depth of the impurity below the surface and its scattering cross section.<sup>100</sup> A later experiment focused on a semiconductor 2DEG by studying a thin layer of InAs grown epitaxially on GaAs.<sup>101</sup> Quasiparticle standing waves have been imaged by STM in the conventional superconductor Nb due to adsorbed magnetic Mn or Gd impurity atoms.<sup>102</sup> The method of using LDOS modulations to reconstruct certain CCE in  $\vec{k}$ -space by analyzing the Fourier transform of the real-space LDOS( $E$ ) image has been employed before on anisotropic metals.<sup>98, 103, 104</sup>

### 3.5.2 Other DOS Modulation Measurements in Cuprates

For the cuprates in general, it had long been proposed that conductance modulations due to quasiparticle scattering should occur, and that both the homogeneous electronic structure and superconducting gap anisotropy could be extracted from measurement of their properties.<sup>105</sup> Dispersing one-dimensional quasiparticle interference patterns have previously been observed in the CuO chains of YBCO<sup>24</sup> due to unknown scatterers (possibly the configuration of the oxygen atoms themselves). However, no attempt was made to Fourier transform these dispersions or to match to a specific band structure in order to find the momentum space properties of the quasiparticles.

Howald *et al.* have observed  $4a_0$  periodic LDOS modulations at  $E = 25$  meV in BSCCO,<sup>106</sup> similar to the  $\vec{q}_1$  modulations reported here, although Howald reports his modulations to be non-dispersing. Howald's modulations have been interpreted as stemming from the simultaneous existence of another electronic ordered-state. This interpretation was based on the apparent static nature of the modulations; however the  $\vec{q}$ -resolution of Howald's study

was not high enough to rule out an unresolved dispersion.

Dung-Hai Lee first proposed the alternative quasiparticle interference explanation<sup>86</sup> for observed DOS modulations in BSCCO, which has been discussed in detail in this chapter. The higher resolution data shown here support the conclusion that observed conductance modulations stem from quasiparticle interference effects. The data in figure 3.15 appears to be due primarily to the quasiparticle interference effect because (i) all modulations have appreciable dispersion, (ii) the dispersions are consistent with scattering between the identified  $\vec{k}$ -space regions of high joint-DOS, and (iii) the evolution of the dispersions with doping is consistent with expected changes in the Fermi surface. Thus, it appears that quasiparticle band-structure effects play the primary role and must be understood before departures from them can be ascribed to other order parameters.

Stronger “checkerboard” modulations around magnetic vortex cores<sup>107</sup> have also been observed, and will be discussed in chapter 4. Dispersion has *not* been detected in the vortex modulations, so it remains very likely that these two phenomena, although similar in appearance, actually stem from quite distinct physical origins.

### 3.5.3 Theories of Quasiparticle Scattering in Cuprates

Byers, Flatte and Scalapino<sup>105</sup> predicted originally in 1993 that quasiparticle scattering would be a useful tool to study the cuprates. Following the first theoretical explanation for our observations and verifying calculation by Wang and Lee,<sup>86</sup> there have been a number of additional theories exploring further details of the problem and providing suggestions for future experiments.

Zhang and Ting<sup>108</sup> commented on the existence of additional  $\vec{q}$ -space peaks. Pereg-Barnea and Franz<sup>109</sup> commented on the importance of coherence factors, and predicted the quasiparticle interference pattern for a possible QED3 phase. Bena *et al.*<sup>110</sup> predicted the quasiparticle interference pattern for a  $d$ -density wave (DDW) phase. Though these calculations provide a valuable ruler against which to measure the continuing search for alternative electronic order, they rely on a limited or unrealistic distribution of scatterers, and have had limited success matching the experimental data so far.

Zhu, Atkinson, and Hirschfeld,<sup>111</sup> working in the ordinary  $d$ -wave superconducting state, were able to incorporate a more realistic distribution of scatterers, including point scatterers to simulate single atom defects, plus a continuously varying background potential to simulate the inherent gap disorder. This more realistic scattering model led to a much closer match between theory and experiment. However, so many parameters had to be tweaked to match

the calculation to experiment, that the authors concluded the  $\vec{q}$ -vectors of the observed interference patterns were more dependent on incoherent scattering effects than on the joint-DOS. While this calculation has done an admirable job matching theory to experiment, the fact remains that the simple joint-DOS calculation of section 3.1.3 also matches the data quite well.

Podolsky *et al.*<sup>95</sup> has also focused attention on coexisting sources of scattering: both random point defects and underlying charge order. The search for underlying order coexisting with random disorder should revolve around the study of highest intensity  $\vec{q}_i$ 's, as shown in figure 3.19. The systematic dependence of these highest-intensity wavevectors on sample doping is suggestive of an increased susceptibility to a doping-dependent ordering. This will be reported in more detail in a future paper by McElroy *et al.*

Vojta and Sachdev originally presented a theory of fluctuating spin density wave (SDW) order in the cuprates.<sup>39</sup> In a following paper, Polkovnikov, Vojta and Sachdev consider dynamic SDW fluctuations as the primary collective degree of freedom and couple it directly to the electrons.<sup>112</sup> The dynamic SDW fluctuations are pinned by disorder and result in a static LDOS modulation at a fixed wavevector whose intensity varies with energy. Following the STM experiments reported here, Polkovnikov, Sachdev and Vojta computed LDOS modulations in a model of electrons scattering off charge density wave order produced by the disorder-induced pinning of the fluctuating SDW, and were able to reproduce “many of the features observed in recent STM experiments.”<sup>113</sup> Specifically, they focused on one dispersing wavevector in reasonable qualitative agreement with our observation of  $\vec{q}_1$ .

Han<sup>114</sup> similarly examines whether the observed dispersing LDOS modulations may be explained by a pinned fluctuating SDW order of fixed wavevector  $\mathbf{Q}$ . While he does find dispersing LDOS modulations resulting from his fixed wavevector starting point, the directions of the dispersions do not all agree with experiment. He concludes that the single  $\mathbf{Q}$  SDW cannot account for our observations.

Andersen<sup>115</sup> shows that the different quasiparticle interference pattern resulting from scattering off two proximate non-magnetic impurities can be used to distinguish between a  $d$ -density wave phase, vs. another form of pairing without superconductivity, in the mysterious pseudogap regime.

Voo *et al.*<sup>116</sup> study a quasiparticle interference model on YBCO which has a  $d_{x^2-y^2+s}$  order parameter resulting from the well-known orthorhombicity of the unit YBCO cell. They conclude that a single impurity scatterer will produce an anisotropic, quasi-one-dimensional quasiparticle interference pattern very similar in appearance to “stripes” but different in origin. Furthermore, they propose a distinguishing test: increasing the concentration of im-

purities would weaken a quasiparticle interference pattern because of the phase incoherence of randomly placed impurities. However, increasing the concentration of impurities should increase “stripe”-pinning and make “stripes” stand out more strongly.

Zhu *et al.*<sup>117</sup> point out the coupling between the magnetic resonance peak at energy  $\sim 40$  meV and the superconducting gap  $\Delta_0$  at an impurity site. The magnetic resonance peak will have little effect on the impurity spectra at low energies, but at energies  $\pm E_1 > \Delta_0$  the impurity will show an alternating modulation pattern of dips and humps in the spectra at  $+E_1$  and  $-E_1$  on-site, nearest neighbor, next nearest neighbor, etc.

Quasiparticle scattering between high joint-DOS regions of  $\vec{k}$ -space has now received direct experimental support as a mechanism for incommensurate, dispersive, spatial modulations of the superconducting electronic structure. Incommensurate, dispersive modulations of the superconducting *magnetic* structure have also been observed in YBCO<sup>66</sup> and LSCO.<sup>118</sup> A related process, similar to our high joint-DOS scattering, in which a quasiparticle is scattered across the Fermi energy into a quasi-hole and vice versa, has been theoretically discussed as a potential explanation.<sup>119, 120, 79, 83</sup> Renewed exploration of such scattering-related explanations for these magnetic phenomena may therefore be appropriate.

### 3.6 Conclusion

In summary, I show via FT-STs that the dominant DOS modulations in optimally doped BSCCO can be well explained as quasiparticle interference. A simple model of the locations in  $\vec{k}$ -space of highest joint-DOS, “the octet model” quantitatively explains the data. There is no need to invoke alternative order parameters or other phases to explain the DOS modulations we observe in optimally doped BSCCO. However, this new experimental technique for looking at the cuprates and simultaneously accessing  $\vec{R}$ -space and  $\vec{k}$ -space quasiparticle information, has prompted a large body of new theoretical work, which in turn provides further promising directions for related experimental study.